Materials Characterization 129 (2017) 288–299

Contents lists available at ScienceDirect

Materials Characterization

journal homepage: www.elsevier.com/locate/matchar

Critical resolved shear stress for slip and twin nucleation in single crystalline FeNiCoCrMn high entropy alloy

Wael Abuzaid[a,*], Huseyin Sehitoglu[b]

[a] Department of Mechanical Engineering, American University of Sharjah, PO Box 26666, Sharjah, United Arab Emirates
[b] Department of Mechanical Science and Engineering, University of Illinois at Urbana-Champaign, 1206 W. Green St., Urbana, IL 61801, USA

ARTICLE INFO

Keywords:
Slip activation
Twin nucleation
High entropy alloys
Hardening
Digital image correlation
Critical resolved shear stress

ABSTRACT

High entropy alloys is an emerging class of materials with superior mechanical properties down to cryogenic temperatures. At 77 K, and unlike traditional metallic alloys, an increase in strength, strain hardening rate, and ductility has been reported. This enhancement in properties has been attributed to the activation of twinning as an additional deformation mechanism at low deformation temperatures. The tendency for the formation of twinning and the hardening response dependence on crystal orientation has not been fully explored. This study is dedicated to explore the deformation evolution across several crystal orientations for the equiatomic FeNiCoCrMn high entropy alloy at room temperature (RT) and 77 K. The works aims to establish the critical resolved shear stresses (CRSS) for slip and twinning and study the orientation and temperature dependence in these magnitudes. The experimental results have revealed a strong temperature dependence in the CRSS for slip, increasing from 56 MPa at RT to 153 MPa at 77 K, with negligible orientation dependence. At 77 K, not all crystal orientations developed twinning even at high levels of deformation. The lack of twinning has been attributed to differences in the hardening response resulting in low stress levels below the twinning CRSS of 153 MPa, as established in this work. No twinning was observed in any of the crystal orientations deformed at room temperature, regardless of the level of hardening and the achieved stresses. Overall, the results discussed in this work enhances our understanding of the local deformation response in single crystalline FeNiCoCrMn high entropy alloy, particularly the nucleation of slip, nucleation of twinning, and the effect of crystal orientation and loading temperature on these deformation mechanisms.

1. Introduction

Traditionally, strengthening of metallic alloys through solid solution or precipitation hardening results in loss of ductility. High entropy alloys (HEA) is an emerging class of metallic alloys which deviates from the common trends by exhibiting high mechanical strength along with significant ductility [1–4]. The simultaneous enhancement in both of these properties extends to extreme cryogenic temperatures where superior toughness measurements, relative to other metallic alloys under similar condition, have been reported. The equiatomic FeNiCoCrMn is one of the most commonly studied HEA due to its remarkable properties at very low temperatures [2,5–12]. In general, the improvement in strength and ductility has been attributed to the activation of twining, in addition to slip, at low temperatures and/or high strains. Most of the reported work, however, has been focused on polycrystalline samples deformed to very high strains and postmortem SEM/TEM analysis [8,9]. The effect of different crystallographic orientations and the role played by grain boundaries can hinder our ability to clearly understand the underlying deformation mechanisms. This work aims to experimentally investigate the deformation evolution of FeNiCoCrMn single crystalline samples deformed at room (~298 K) and cryogenic temperatures (77 K). By collecting high resolution full field strain and orientation measurements, we pinpoint the critical stresses for the activation of slip and twinning nucleation, highlight the different deformation mechanisms at various loading levels, and investigate the hardening response in the presence of slip and/or twinning. Overall, the work provides a deeper insight into the local deformation mechanisms in FeNiCoCrMn HEA and enhances our understanding of the role played by deformation twinning in improving the ductility at low temperatures.

The equiatomic FeNiCoCrMn HEA has a stable single phase with face-centered cubic (FCC) crystal structure. The deformation of this alloy takes place primarily by slip on the {111} ⟨110⟩ slip systems [5]. At low deformation temperatures (*i.e.*, 77 K) and high strains (> 20%), several researchers have reported deformation twinning to operate in addition to slip [2,7]. The strengthening effect of twinning is

* Corresponding author.
E-mail address: wabuzaid@aus.edu (W. Abuzaid).

http://dx.doi.org/10.1016/j.matchar.2017.05.014
Received 17 March 2017; Received in revised form 9 May 2017; Accepted 10 May 2017
Available online 12 May 2017

similar to what is typically observed in twinning induced plasticity steels (TWIP steels) where twin-slip interaction results in strain hardening and consequently improved ductility by obstructing the formation of necking [13–16]. The activation of slip/twinning is obviously orientation dependent and the initiation stresses will differ from crystal to crystal. The wealth of experimental work and the corresponding analysis obtained from polycrystalline samples provide detailed analysis into the role played by twining in the deformation response of FeNiCoCrMn. However, the effect of crystal orientation is smeared and it becomes very challenging to determine the critical stresses for slip/twinning nucleation [17]. For example, Laplanche has reported a discrepancy between the critical resolved shear stress for twinning (CRSS) obtained from the critical twinning stress (obtained from a polycrystalline sample and using a Taylor factor of 3.06) and theoretical values obtained from density functional theory [8]. With single crystalline samples and detailed electron backscattering diffraction (EBSD) orientation data and high resolution digital image correlation (DIC) strain measurements, the CRSS can be pinpointed without ambiguity [18]. In addition, the tendency of different orientations to slip and/or twinning can be investigated at different stages of deformation; thus providing means to assess the validity of Schmid law to predict slip and twinning for FeNiCoCrMn HEA.

The utilization of high resolution DIC and EBSD crystal orientation measurements, both covering the same region on the sample's surface, has proven to be very useful in determining the CRSS for the nucleation of slip or twinning in single crystalline metallic alloys. However, as the high resolution DIC measurements require reference and deformed images to be captured in the optical microscope at high magnifications, the DIC measurements are limited to ~3% total plastic strain. Further deformation will lead to significant surface distortions which would ultimately hinder the ability to capture *focused* deformed images. As the emphasis in this work is on both, the critical nucleation stresses early in the deformation, and the changes taking place at very high strains (*e.g.*, hardening and activation of twinning), there is a need to extend the range at which DIC measurements can be collected on the same sample. Through incremental loading steps followed by a sequence of polishing and re-establishing *ex-situ* DIC pattern, we were able to map out the entire response of each sample under consideration up to ~40% strain. The incremental full field data yields detailed information of deformation *between* loading steps. By focusing on the same region of interest (sample edges utilized in this work for alignment), such analysis is advantageous for capturing the factors influencing the hardening response and the activation of twinning at potentially high strains as will be shown in the current study.

In summary, this study is focused on studying the local deformation response of single crystalline FeNiCoCrMn HEA across a wide range of crystal orientations (⟨111⟩ , ⟨149⟩ , ⟨122⟩ , and ⟨123⟩). We pinpoint the activation of slip and twinning at different stages of deformation at room temperature (RT) and 77 K. We further asses the validity of the Schmid law to predict the activation of deformation twinning based on the determined CRSS and the considered crystal orientations. Finally, and by capturing the underlying deformation mechanisms, we shed further insight into the interactions taking place during loading and their impact on the observed hardening response and discuss the observations as they relate to the formation of localized response (*i.e.*, necking) and the formation of twinning.

2. Materials and Methods

Single crystal ingot of equiatomic FeNiCoCrMn was grown using the Bridgman technique in He atmosphere. Homogenization of the crystal was conducted at 1200 °C for 24 h followed by quenching in oil. Dogbone tension samples with 3 × 1.5 mm gauge section were electric discharge machined from the ingot with the loading axis along the ⟨111⟩ , ⟨149⟩ , ⟨122⟩ , and ⟨123⟩ crystallographic directions. The crystal orientations were determined using EBSD as detailed in the Appendix. Prior to loading, all samples were solution heat treated at 1100 °C for 1 h, followed by oil quenching, and subsequent polishing using *SiC* paper to prepare the surface for high resolution *ex-situ* DIC measurements following the procedure detailed in [19]. Reference and deformed images for full field strain measurements were collected using optical microscopy, *ex-situ*, at 5 × magnification which corresponds to an imaging resolution of ~0.88 μm/pixel. A single image field of view was 1.41 × 1.05 mm. To cover the entire width of the sample with the selected high resolution setting, 3 images were captured across the width of the sample with ~30% overlap. Two rows of images were collected to increase the size of the region monitored with high resolution DIC (region of interest ~3 × 2 mm). The DIC correlations were conducted on the original images with results stitching following the procedure detailed in [20].

An Instron servo hydraulic load frame was used for tensile loading, in displacement control, with an average strain rate of $1.67^{-4}\,s^{-1}$. Sample alignment was achieved through a set of matching holes in the load frame grips and in both ends of the sample (see sample schematic in the Appendix). Prior to final clamping, alignment pins were inserted through the holes in the sample and grips. Each sample was incrementally loaded up to a total strain of ~40%. The specified loading increments varied from sample to sample and was adjusted depending the observed response and hardening behavior. At the end of each loading increment, the samples were removed from the load frame to collect deformation images in the optical microscope. To enable continued high resolution *ex-situ* DIC data collection, additional surface polishing was required to re-establish a good quality pattern after each loading increment. Therefore, the reported DIC measurements represent the incremental accumulation of strain between loading cycles and not the total accumulated strains. Experiments were conducted at two different temperatures, room temperature (RT ~ 298 K) and 77 K where the specimen, grips, and extensometer (for data collection only and not for control) were all submersed in liquid nitrogen. For the RT experiments, *in-situ* DIC measurements were collected during loading for the first increment only to help establish the critical stress for slip activation. At 77 K, such measurements were not possible as the samples were completely submersed in liquid nitrogen, thus leaving no access to image the surface *in-situ*.

3. Results and Analysis

Fig. 1 shows the stress-strain response for a ⟨111⟩ sample loaded to ~5% strain (one loading increment). *In-situ* DIC images were collected every 2 s during loading with an imaging resolution of 2.1 μm/pixel. The region of interest within the 1600 × 1200 pixel single image field of view was 3 × 2.5 mm. Selected DIC contour plots shown as insets in the figure represent the normal strains along the loading direction (henceforward referred to as normal strains) at different applied strain levels (full field *in-situ* DIC). The clear strain bands after unloading the sample represent traces of slip along the $(\bar{1}11)$ slip plane. Tracing back the point on the stress-strain curve where the DIC contour plots show activation of these strain bands defines the critical stress for slip nucleation (*i.e.*, 170 MPa as shown in Fig. 1). Out of the three slip systems sharing the $(\bar{1}11)$ slip plane, the highest Schmid factor was 0.31 as shown in Table 1. Using the highest Schmid factor (determined using the original crystal orientation) and the critical nucleation stress, the CRSS for activation of slip was calculated to be τ_S = 53 MPa. We note here that a perfectly aligned ⟨111⟩ crystal would have yielded a maximum Schmid factor of 0.27 on 6 different systems. The deviation from the expected results, for a perfectly aligned crystal, and the values reported in Table 1 arises from the fact that the experimentally measured crystal orientation, determined using EBSD and reported in the Appendix, was used for the calculation of the Schmid factors. In addition, as the EBSD data collection and sample loading were on two different frames, some misalignment error is expected. Based on the points stated above, the

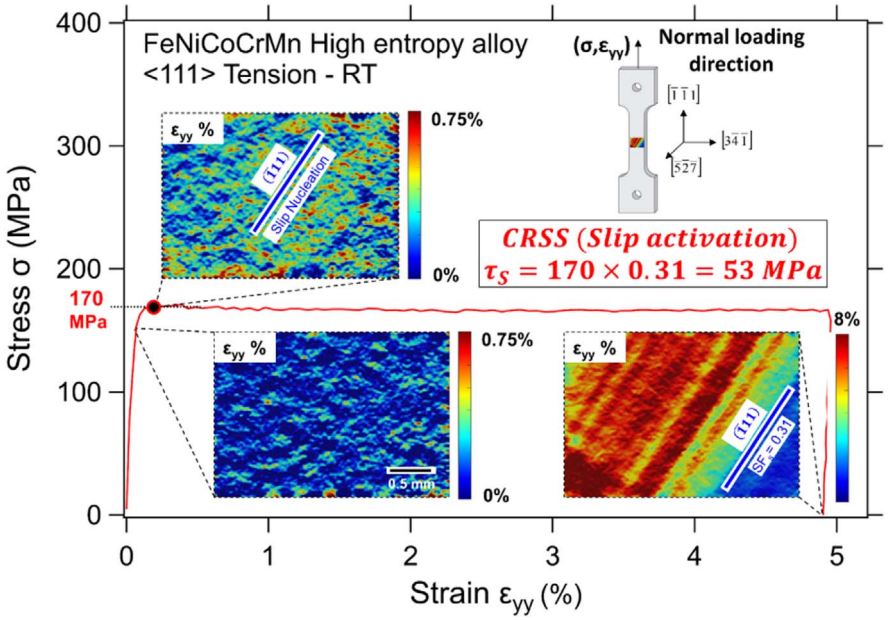

Fig. 1. (a) Stress-strain response for a ⟨111⟩ single crystal loaded at room temperature. *In-situ* DIC contour plots, shown as insets, represent the normal strain fields obtained *in-situ* during loading. Activation of slip on the $(\bar{1}11)$ was observed. The critical stress marking the onset of slip activation and the Schmid factor for the observed slip system were used to determine the CRSS for slip activation.

Table 1
Schmid factors for ⟨111⟩ single crystal (based on original crystal orientation from EBSD orientation data). The activated slip and twin systems for the samples discussed in Figs. 2 and 4 are highlighted in the table.

Slip system	Schmid factor - slip	Schmid factor - twin	Twin system
$(111)[\bar{1}01]$	0.32	− 0.20	$(111)[\bar{2}11]$
$(111)[1\bar{1}0]$	0.03	− 0.15	$(111)[1\bar{2}1]$
$(111)[0\bar{1}1]$	0.29	0.35	$(111)[11\bar{2}]$
$(\bar{1}\bar{1}1)[0\bar{1}\bar{1}]$	0.01	− 0.08	$(\bar{1}\bar{1}1)[2\bar{1}1]$
$(\bar{1}\bar{1}1)[\bar{1}0\bar{1}]$	0.08	0.03	$(\bar{1}\bar{1}1)[\bar{1}21]$
$(\bar{1}\bar{1}1)[1\bar{1}0]$	0.07	0.05	$(\bar{1}\bar{1}1)[\bar{1}\bar{1}\bar{2}]$
$(1\bar{1}1)[0\bar{1}\bar{1}]$	0.00	0.25	$(1\bar{1}1)[\bar{2}\bar{1}1]$
$(1\bar{1}1)[\bar{1}01]$	0.21	− 0.13	$(1\bar{1}1)[121]$
$(1\bar{1}1)[\bar{1}\bar{1}0]$	0.21	− 0.12	$(1\bar{1}1)[1\bar{1}\bar{2}]$
$(\bar{1}11)[\bar{1}0\bar{1}]$	0.03	− 0.19	$(\bar{1}11)[211]$
$(\bar{1}11)[\bar{1}\bar{1}0]$	**0.31**	**0.34**	$(\bar{1}11)[\bar{1}\bar{2}1]$
$(\bar{1}11)[0\bar{1}1]$	**0.28**	− 0.14	$(\bar{1}11)[\bar{1}1\bar{2}]$

observation of slip on the system with 0.31 Schmid factor and not on the system with the maximum 0.32 Schmid factor is not of much significance.

Fig. 2 shows the stress-strain response for a ⟨111⟩ sample loaded incrementally to ~40% strain at room temperature. At the end of each loading increment (*i.e.*, D1-D12 as marked in Fig. 2a) the sample was removed from the load frame for *ex-situ* DIC measurements. As the sample had to be polished to re-establish a smooth surface for high resolution *ex-situ* DIC prior to additional loading, the reported stress-strain *response* doesn't represent either an *engineering* or a *true* stress strain curve. The reason is that the sample's cross section had to measured and adjusted after each loading increment. This process was necessary to collect the high resolution DIC at different levels of deformation. The high resolution measuring capability would have been otherwise limited to 3% at which significant surface changes prevents further DIC analysis. The stress jumps observed in some of the loading increments (*e.g.*, D10 in Fig. 2a) resulted from this process. Selected contour plots of the normal strain field, ε_{yy} along the loading direction, are shown in Fig. 2b. Each one of the contour plots reports the incremental response between the end of the prior loading cycle and the current deformed state. At early stages of deformation, the full field DIC data conveys single slip as depicted from the contour plot at D1 in Fig. 2b (*i.e.*, 3% plastic strain). The slope of the observed slip bands matches the traces created by the $(\bar{1}11)$ slip plane on the sample's surface. The activated slip system can be either the $(\bar{1}11)[\bar{1}\bar{1}0]$ or the $(\bar{1}11)[0\bar{1}1]$ since both have similar Schmid factors as listed in Table 1. Single slip continued to dominate the response (only primary slip was observed at D5) up to ~25% where traces of slip on the (111) started to emerge as shown in D7, and more clearly in D9, in Fig. 2b. A significant hardening associated with slip-slip interaction accompanied the activation of secondary slip as expected. Fig. 3a-b highlights a few examples showing clear slip-slip interactions. Another feature that was observed in the contour in Fig. 3, taken at very high strain corresponding to D11 and D12, is the emergence of curvatures or steps in the strain bands as marked in Fig. 3. Based on orientation measurements after deformation, no clear signs of twinning were observed for this sample as shown in the EBSD map (Fig. 3c) and inverse pole figure (IPF) (Fig. 3d).

Another ⟨111⟩ sample was loaded incrementally but at 77 K as opposed to the room temperature case reported in Fig. 2. The incremental stress-strain response is presented in Fig. 4a. Noticeable stress drops were observed early in the deformation of this sample which is a likely indication of twin nucleation. These drops were also accompanied with an audible clicking sound during loading. The deformed images captured in the microscope revealed pronounced local deformation as shown in Fig. 4b. Although the total accumulated strain at the end of deformed state D1, marked in Fig. 4a, was about 3%, the significant local deformation prohibited any DIC measurements. These observations (*i.e.*, pronounced and sudden stress drop during loading and significant local deformation) are all indicative of twinning. The traces observed in the optical image matches that of the $(\bar{1}11)$ crystallographic plane. The twinning Schmid factors for this crystal are shown in Table 1. Based on the observed $(\bar{1}11)$ traces and the Schmid factor magnitudes, the observed twining is most probably the $(1\bar{1}1)[\bar{1}\bar{2}1]$ twin system. DIC measurements collected in a subsequent loading showed a highly localized response with very high strains in twinned regions (see Fig. 4c). As twining in this case was accompanied with a very clear stress drop, that stress can be used to depict the critical resolved shear stress (CRSS) for twinning τ_T. The first stress drop occurred at ~450 MPa as shown in Fig. 4a. Based on trace analysis and DIC measurements, the activated twin system was determined to be

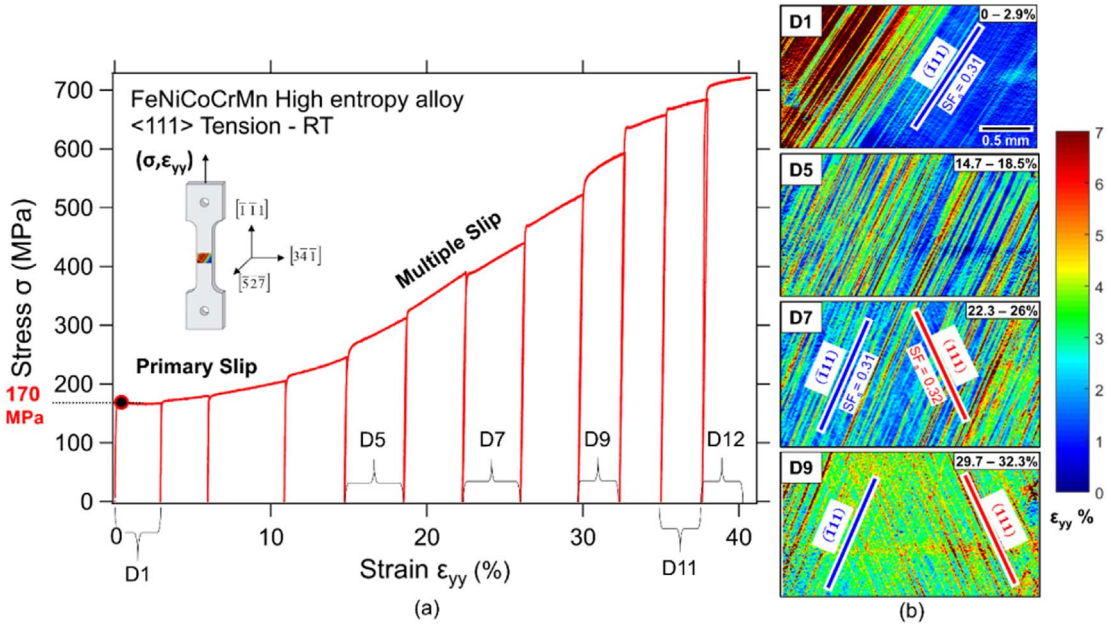

Fig. 2. (a) Incremental stress-strain response for a ⟨111⟩ single crystal loaded at room temperature. (b) Selected contour plots showing the normal strain fields ε_{yy} at different loading levels. Notice that the reported contour plots represent the strain accumulation during the reported loading increment only and not the total strain accumulation.

the $(1\bar{1}1)[\bar{1}\bar{2}1]$ twin system which has a Schmid factor of 0.34. Therefore, the CRSS for twinning was found to be $\tau_T \cong 153$ MPa. Additional strain bands with a slope matching the trace of the (111) plane were also detected in Fig. 4c. Based on the Schmid factors reported in Table 1, either slip (2 systems with high Schmid factors) or twinning (one system with high Schmid factor) are possible. However, based on the low levels of local strains in these bands, compared to the twinned regions, and the absence of stress drops and/or the significant local deformation usually accompanying twinning, we associate these traces with activation of primary slip.

Fig. 5a shows the stress-strain response for a ⟨149⟩ sample loaded incrementally to ~38% strain at room temperature. Based on original crystal orientation, obtained from EBSD, the Schmid factors for slip and twinning were calculated as shown in Table 2. Both the $(111)[\bar{1}01]$ and the $(\bar{1}11)[\bar{1}0\bar{1}]$ slip systems have high Schmid factors (0.50 and 0.47 respectively). Traces of these two slip systems were clearly detected in the *ex-situ* DIC results as shown in ε_{yy} normal strain fields presented in Fig. 5b. The deformation was not homogeneous, however, as two distinct regions emerged where the deformation was dominated by only one of the systems in one area, and the other system in the neighboring region. A distinct interface separating both regions can be discerned in both, the optical deformed images and the DIC contour plots as marked in Fig. 5b. EBSD data collected after 3% strain (D1 in Fig. 5) did not reveal any orientation difference that would trigger such a response (*i.e.*, it is not a bicrystal). To further investigate the emergence of this feature, EDX analysis was conducted across the entire width of the

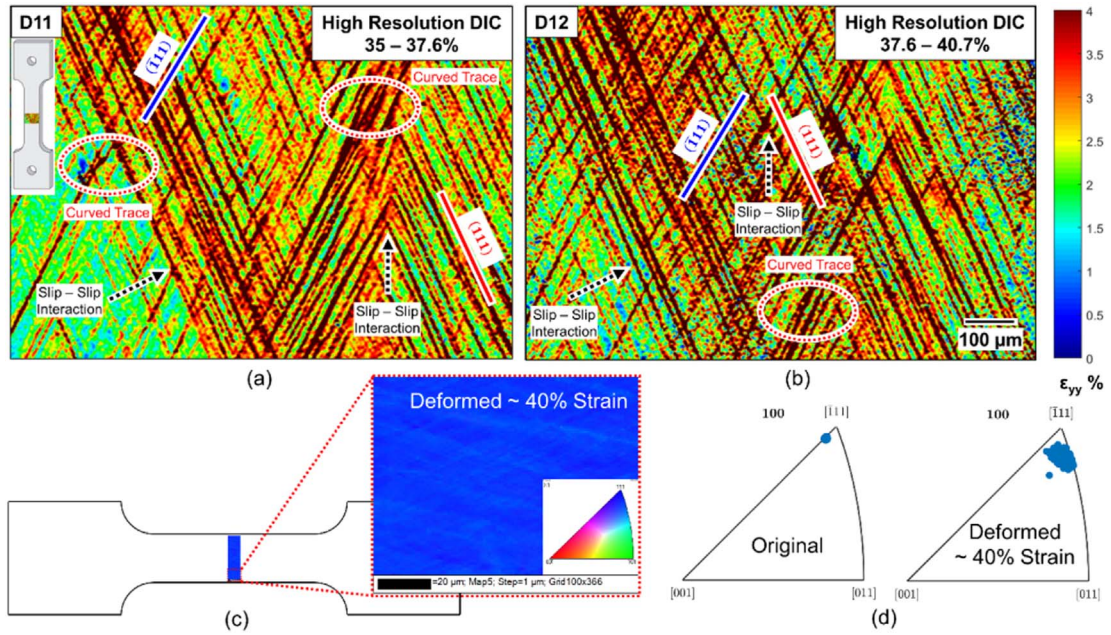

Fig. 3. (a)-(b) Contour plots of the normal strain field ε_{yy} for deformed states D11 and D12 (marked in Fig. 2a). The strain bands show clear locations for slip-slip interactions, marked with black arrows, and bands with curvature/steps as marked with red circles. (c) EBSD map taken across the width of the sample (same region covered with DIC). The corresponding inverse pole figure is shown in (d). (For interpretation of the references to colour in this figure legend, the reader is referred to the web version of this article.)

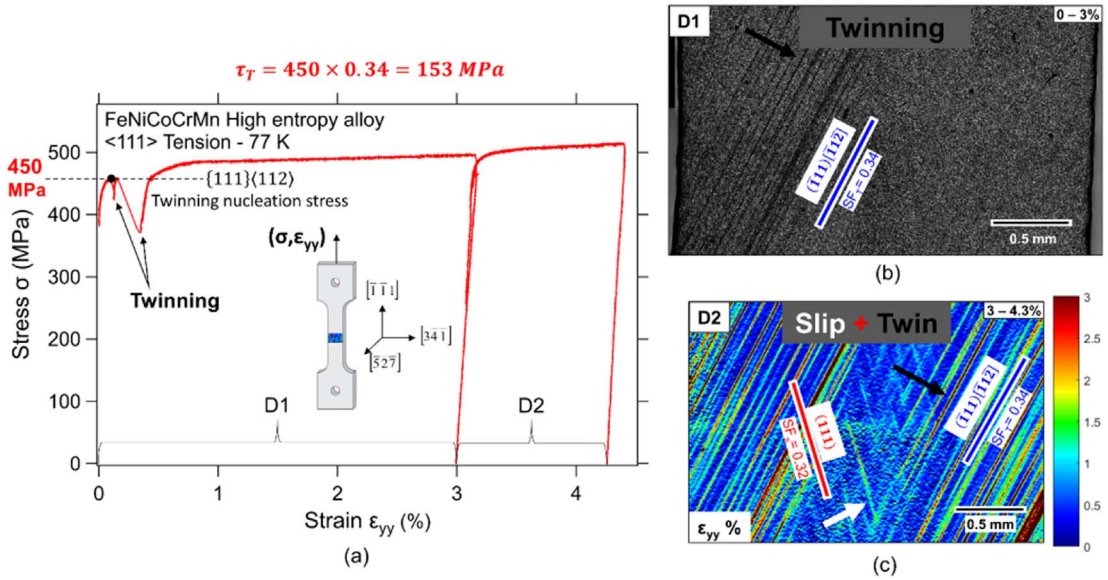

Fig. 4. (a) Incremental stress-strain response for a ⟨111⟩ single crystal loaded at 77 K. (b) Deformed region of interest at the end of the first loading cycle D1. The shown optical image is composed of six optical images captured in the microscope and stitched. (c) Contour plot of the normal strain field ε_{yy} for deformed state D2.

sample, thus shuttling between the two distinct regions observed in the optical and DIC images. The EDX results, presented in Fig. 6, do not point to a clear correlation between the observed deformation and the compositional homogeneity of the crystal. No signs of twining were observed for this orientation during room temperature deformation.

The previous orientation, ⟨149⟩, was also investigated at 77 K. The stress-strain response obtained from incrementally loading a sample at 77 K is shown in Fig. 7a. The DIC contour plot of the ε_{yy} normal strains at D1 (shown as inset in Fig. 7a) displayed similar features as compared to the room temperature case. Activation of both the slip systems with the highest Schmid factors was observed; the $(111)[\bar{1}01]$ and $(\bar{1}11)[\bar{1}0\bar{1}]$ slip systems. With continued loading, significant localization in the plastic strains was seen in the DIC contour plots as shown in Fig. 7c. These localizations were associated with slip-slip interaction primarily at the interface separating the two regions with dissimilar primary slip. Necking in the gauge area also took place as shown in Fig. 7b. The deformation in the necked region, although localized, did not display the formation of the two distinct regions and was therefore more homogeneous. This was confirmed by subsequent

Table 2
Schmid factors for ⟨149⟩ single crystal (based on original crystal orientation from EBSD orientation data). The activated slip systems for the samples discussed in Figs. 5 and 7 are highlighted in the table.

Slip system	Schmid factor - slip	Schmid factor - twin	Twin system
$(111)[\bar{1}01]$	**0.50**	0.44	$(111)[\bar{2}11]$
$(111)[1\bar{1}0]$	0.27	− 0.03	$(111)[1\bar{2}1]$
$(111)[0\bar{1}1]$	0.23	− 0.42	$(111)[11\bar{2}]$
$(\bar{1}\bar{1}1)[0\bar{1}\bar{1}]$	0.29	0.03	$(\bar{1}\bar{1}1)[2\bar{1}1]$
$(\bar{1}\bar{1}1)[\bar{1}0\bar{1}]$	0.17	0.23	$(\bar{1}\bar{1}1)[\bar{1}21]$
$(\bar{1}\bar{1}1)[1\bar{1}0]$	0.11	− 0.27	$(\bar{1}\bar{1}1)[\bar{1}\bar{1}\bar{2}]$
$(1\bar{1}1)[0\bar{1}\bar{1}]$	0.20	0.05	$(1\bar{1}1)[\bar{2}\bar{1}1]$
$(1\bar{1}1)[\bar{1}01]$	0.14	0.15	$(1\bar{1}1)[121]$
$(1\bar{1}1)[\bar{1}\bar{1}0]$	0.05	− 0.20	$(1\bar{1}1)[1\bar{1}\bar{2}]$
$(\bar{1}11)[\bar{1}0\bar{1}]$	**0.47**	0.39	$(\bar{1}11)[211]$
$(\bar{1}11)[\bar{1}\bar{1}0]$	0.21	0.03	$(\bar{1}11)[\bar{1}\bar{2}1]$
$(\bar{1}11)[0\bar{1}1]$	0.26	− 0.42	$(\bar{1}11)[\bar{1}1\bar{2}]$

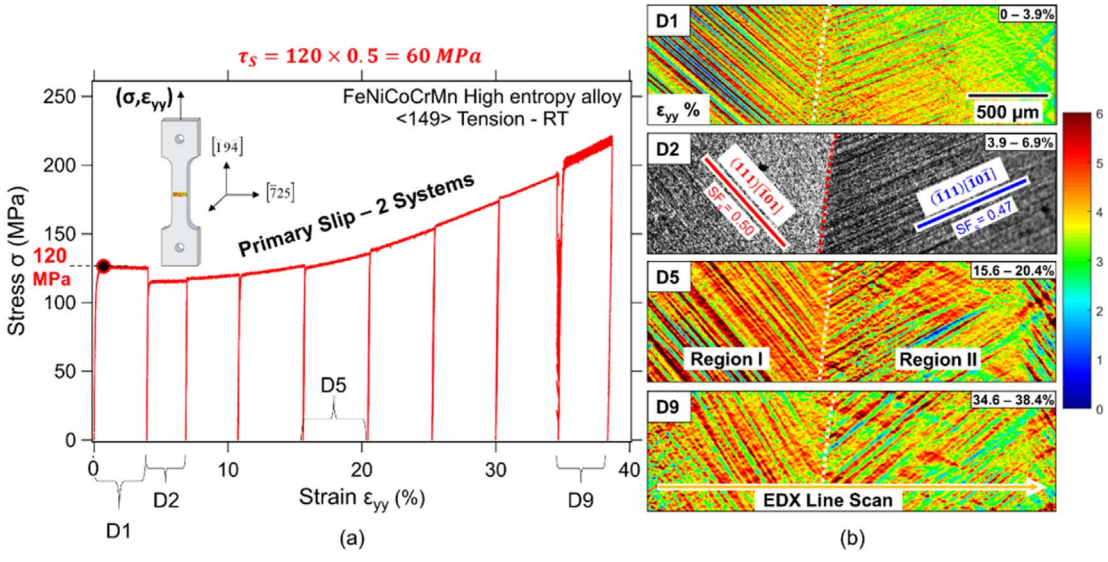

Fig. 5. (a) Incremental stress-strain response for a ⟨149⟩ single crystal loaded at room temperature. (b) Selected contour plots showing the normal strain fields ε_{yy} along the loading at different loading levels. Using the original crystal orientation, the observed strain bands were indexed showing the activated slip planes.

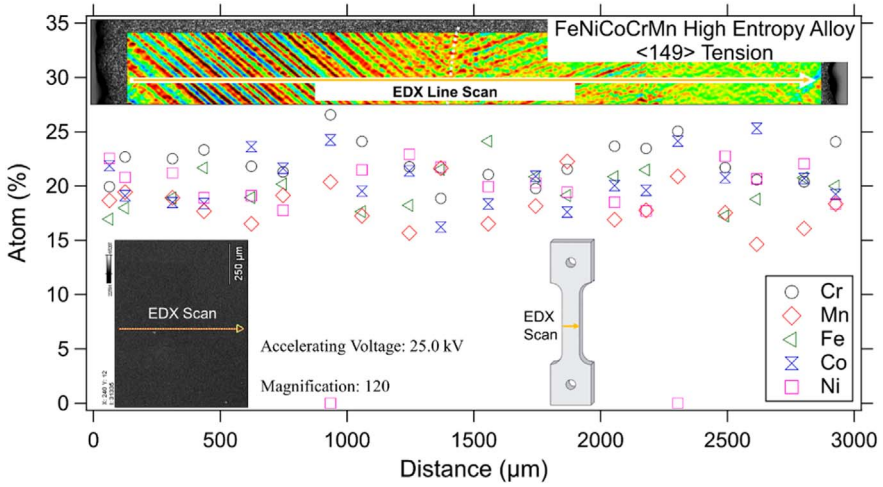

Fig. 6. (a) EDX line scan across the width of the ⟨149⟩ sample presented in Fig. 5. The inset shows a sample DIC contour plot.

EBSD data collected after ~32% plastic strain as shown in Fig. 8. EBSD orientation map and IPF in the necked area were more homogenous compared to the two regions shown at the bottom of the sample in Fig. 8b. Clearly each one of these two regions, Regions I and II as marked in the inset in Fig. 7a, evolved differently during deformation resulting in relatively significant orientation difference compared to the area where necking was observed. We note that such orientation difference did not exist before deformation. This observation is discussed further in Section 4 of the manuscript.

Fig. 9 shows the stress-strain response for a ⟨122⟩ single crystal loaded in tension at 77 K. Early in the deformation behavior of this sample, primary slip dominated the response. The observed slip bands in the D1 DIC contour plots presented Fig. 9b matched the traces created by the (111) slip plane on the sample's surface. Two slip systems sharing this slip plane have high Schmid factor (0.41) as shown in Table 3. With continued loading, another strain band emerged with high localized strains. The strain bands can be discerned in the D3 contour plots in Fig. 9b. This type of localization dominated the response beyond D3 (see D6 in Fig. 10). EBSD analysis after deformation (~38% strain) revealed significant twining on the $(1\bar{1}1)$ as shown in Fig. 10b. Based on the orientation measurements, the high strain bands on the $(1\bar{1}1)$ plane that were detected first at D3 and dominated the response as seen in D6 are associated with twinning. We note that RT experiments were not conducted for this orientation. Based on the previous results for the ⟨111⟩ and ⟨149⟩ samples, the RT condition for tension along ⟨122⟩, and later for the ⟨123⟩ sample, was not expected to show twining. As the CRSS for slip activation and its temperature dependence were already captured from the previous results, we decided to focus on the 77 K cryogenic temperature condition which has a higher probability for the nucleation of twinning compared to RT.

The final orientation considered in this study was ⟨123⟩. The stress-strain response from incremental tensile loading at 77 K is shown in Fig. 11a. The full field strain measurements revealed primary slip activity on the $(111)[\bar{1}01]$ slip system, which has the highest Schmid factor (see Table 4). With continued loading, see D3 in Fig. 11b, strain bands from different crystallographic planes were not observed and the deformation continued to be dominated by slip on the (111) plane.

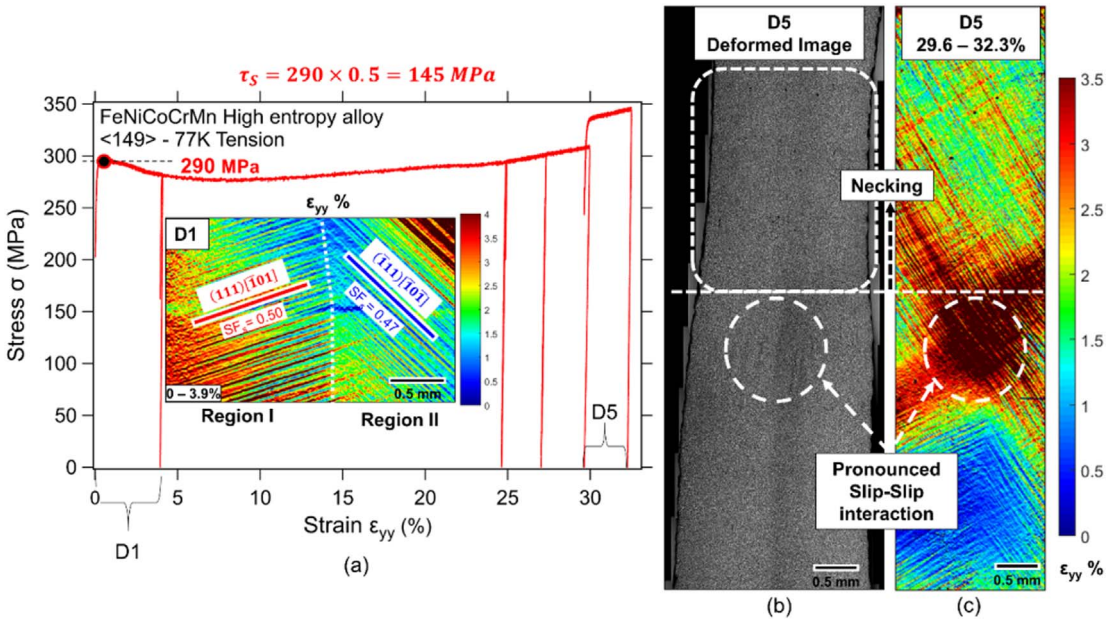

Fig. 7. (a) Incremental stress-strain response for a ⟨149⟩ single crystal loaded at 77 K. (b) Optical microscope image of the deformed sample at the end of D5. The sample necked as marked in the image. (c) Contour plots showing the normal strain fields ε_{yy} for D5. Significant localization was observed which was attributed to slip-slip interaction around the interface separating Regions I & II which had dissimilar primary slip activity as shown in (a).

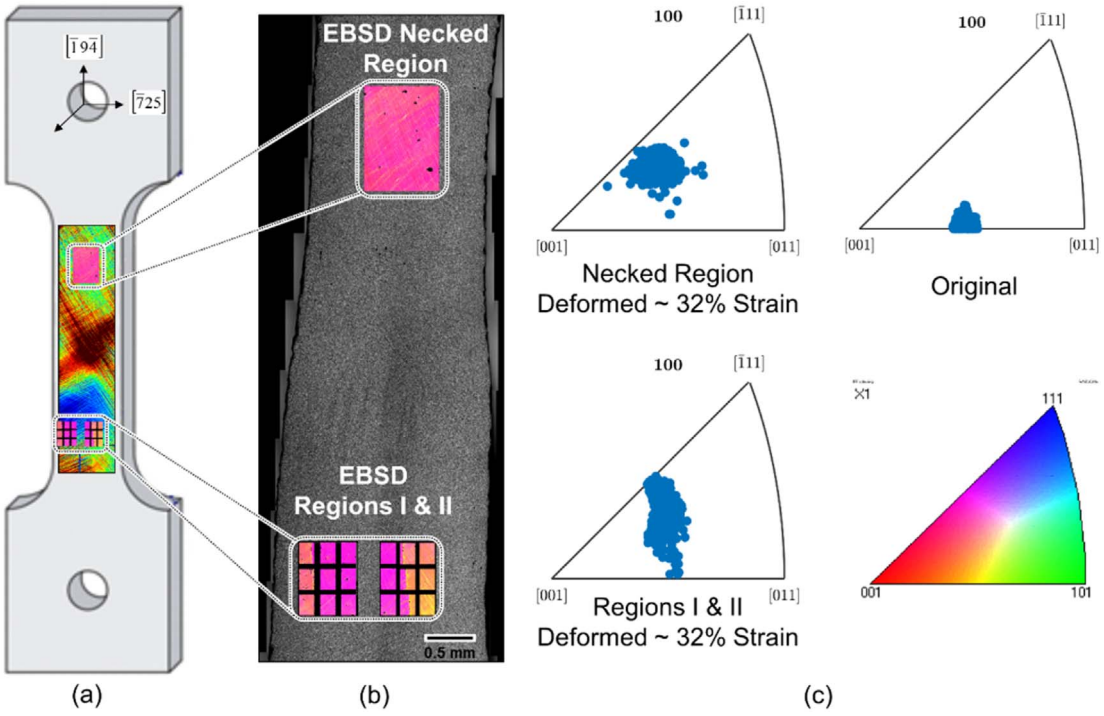

Fig. 8. (a) Schematic of the ⟨149⟩ tension sample presented in Fig. 7. The DIC region and the relative locations where EBSD data was collected are marked. (b) EBSD orientation data collected from the necked area and sample Regions I and II. The maps are overlaid on the deformed image at the end of D5 shown in Fig. 7a. (c) The corresponding IPFs for the EBSD maps shown in (b).

Subsequent EBSD analysis did not point to the presence of large scale twinning as observed previously for the ⟨122⟩ sample. The EBSD map is presented in Fig. 12, notice that the IPF in Fig. 12c indicate that significant lattice rotation took place for this orientation. The EBSD map also shows small islands, some highlighted with white arrows in Fig. 12b. Higher resolution EBSD conducted for selected regions having these features showed primarily a misorientation of about 3° relative to the surrounding material with no signs of twinning

4. Discussion

Based on crystal orientation measurements, trace/strain band analysis, and high resolution DIC data, the CRSS for the activation of slip has been experimentally determined for multiple crystal orientations and deformation temperatures. Table 5 lists the experimentally determined critical stresses and the calculated CRSS for slip activation τ_S. The determined magnitudes are consistent among orientations but differ based on the loading temperature. A similar observation has been made by Patriarca from compression experiments on [5$\bar{9}$1] single crystals [17]. This dependence is most probably attributed to differences in the frictional stress (*i.e.*, lattice resistance to dislocation motion) upon changing temperature. Wu et al. provide a detailed discussion of this point where they attribute the temperature dependence in yield stress (polycrystalline equiatomic HEA) to temperature

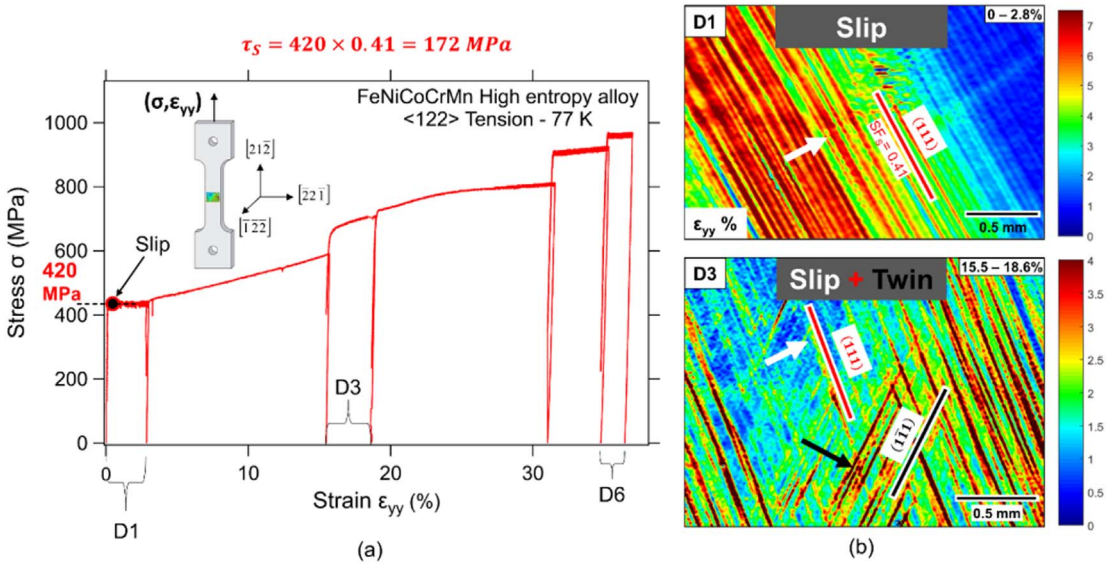

Fig. 9. (a) Incremental stress-strain response for a ⟨122⟩ single crystal loaded at 77 K. (c) Selected contour plots showing the normal strain fields ε_{yy} along the loading for D1 and D3. The localizations and strain bands in D1 were associated slip activity on the (111) slip plane. In D3, the strain localizations on the (1$\bar{1}$1) plan are due to the activation of twining (see also Fig. 10).

Table 3
Schmid factors for ⟨122⟩ single crystal (based on original crystal orientation from EBSD orientation data). The activated slip and twin systems for the samples discussed in Figs. 9 and 10 are highlighted in the table.

Slip system	Schmid factor - slip	Schmid factor - twin	Twin system
$(111)[\bar{1}01]$	**0.41**	− 0.23	$(111)[\bar{2}11]$
$(111)[1\bar{1}0]$	0.00	− 0.24	$(111)[1\bar{2}1]$
$(111)[0\bar{1}1]$	**0.41**	0.47	$(111)[11\bar{2}]$
$(\bar{1}\bar{1}1)[0\bar{1}\bar{1}]$	0.23	− 0.13	$(\bar{1}\bar{1}1)[2\bar{1}1]$
$(\bar{1}\bar{1}1)[\bar{1}0\bar{1}]$	0.22	− 0.13	$(\bar{1}\bar{1}1)[\bar{1}21]$
$(\bar{1}\bar{1}1)[1\bar{1}0]$	0.00	0.26	$(\bar{1}\bar{1}1)[\bar{1}\bar{1}2]$
$(1\bar{1}1)[0\bar{1}\bar{1}]$	0.05	**0.19**	$(1\bar{1}1)[\bar{2}\bar{1}1]$
$(1\bar{1}1)[\bar{1}01]$	0.14	− 0.13	$(1\bar{1}1)[121]$
$(1\bar{1}1)[\bar{1}\bar{1}0]$	0.19	− 0.05	$(1\bar{1}1)[1\bar{1}\bar{2}]$
$(\bar{1}11)[\bar{1}0\bar{1}]$	0.04	− 0.13	$(\bar{1}11)[211]$
$(\bar{1}11)[\bar{1}\bar{1}0]$	0.18	0.18	$(\bar{1}11)[\bar{1}\bar{2}1]$
$(\bar{1}11)[0\bar{1}1]$	0.14	− 0.05	$(\bar{1}11)[\bar{1}1\bar{2}]$

dependence in the Peierls–Nabarro stress [21]. Such an effect will manifest itself on the CRSS for slip activation as observed in this work. Based on this discussion, the typical increase in yield strength reported for polycrystalline FeNiCoCrMn HEA at 77 K cannot be induced by the introduction of twinning as an additional deformation mechanism. The fact that not all the orientations studied in this work displayed twinning when deformed at 77 K and that twinning was preceded by considerable slip activity in the ⟨122⟩ crystal supports this conclusion.

As for the CRSS for twin nucleation τ_T, only one experimental results was available for the nucleation stress, which was from the ⟨111⟩ sample loaded at 77 K. The other sample where twinning was also clearly observed (*i.e.*, the ⟨122⟩ sample at 77 K) does not allow for precise calculation of the twinning stress as the deformation was initially dominated by slip and therefore the exact point or onset of twinning could not be picked. However, we note that based on the Schmid factor for the observed twin system (0.2 as listed in Table 3) and the stress levels during the third loading cycle D3 (notice that twinning was observed at the end of D3 as shown in Fig. 9), the CRSS would be in the range reported from the ⟨111⟩ sample. Since twinning (at the microscale) was not observed in any of the samples tested at room temperature, no data is available to assess any temperature dependence in the CRSS for twinning nucleation τ_T. The wealth of literature on deformation twinning seems to support that twinning in FCC metals is either temperature independent or has a weak temperature sensitivity [22]. However, it is plausible that HEAs will deviate from this trend, as it does for the case of slip. An increase in the CRSS for twin nucleation at room temperature can explain the lack of twinning activity for the ⟨111⟩ sample which displayed significant hardening and high stresses on the order of the CRSS where twinning was clearly detected at 77 K. Limited studies are available addressing the question of whether the CRSS for twin nucleation is temperature dependent in the case of HEAs. In recent work by Laplanche et al., the CRSS for twinning was reported to be temperature insensitive for polycrystalline FeNiCoCrMn [8]. Due to differences in the hardening response with different deformation temperatures, twinning in their case was observed close to fracture for the 293 K case. The stress determined in their work was, however, much higher than the CRSS obtained at 77 K in this work (235 compared to 155 MPa in this study). The fact that a polycrystalline sample and Taylor factor analysis was used to establish the stress may contribute to the discrepancy with the results from single crystalline samples. This aspect still requires additional research to determine if there is any temperature dependence in the CRSS for twinning nucleation from single crystalline samples.

Another important question is raised based on the previous observations; can the CRSS for twin nucleation and the Schmid law explain the lack of obvious twinning in many of the deformed samples? Based on what has been typically discussed in the literature, deformation at 77 K or at strains in excess of 20% should have been accommodated by deformation twinning in addition to slip. Table 6 lists all the crystal orientations, the maximum stress levels achieved during loading, and the highest possible resolved shear stress for the twin system having the highest Schmid factor (calculated using the original crystal orientation, not necessarily observed twin system). The two samples where clear twinning was reported both have obviously resolved shear stresses that exceeds the CRSS of 155 MPa. The ⟨149⟩ samples, both at room temperature and 77 K, had maximum resolved stresses that were below the experimentally determined τ_T in this study, which would explain why twining was not observed in these two conditions. The maximum achieved resolved shear stress for the ⟨123⟩ sample barely reached the CRSS for twinning nucleation

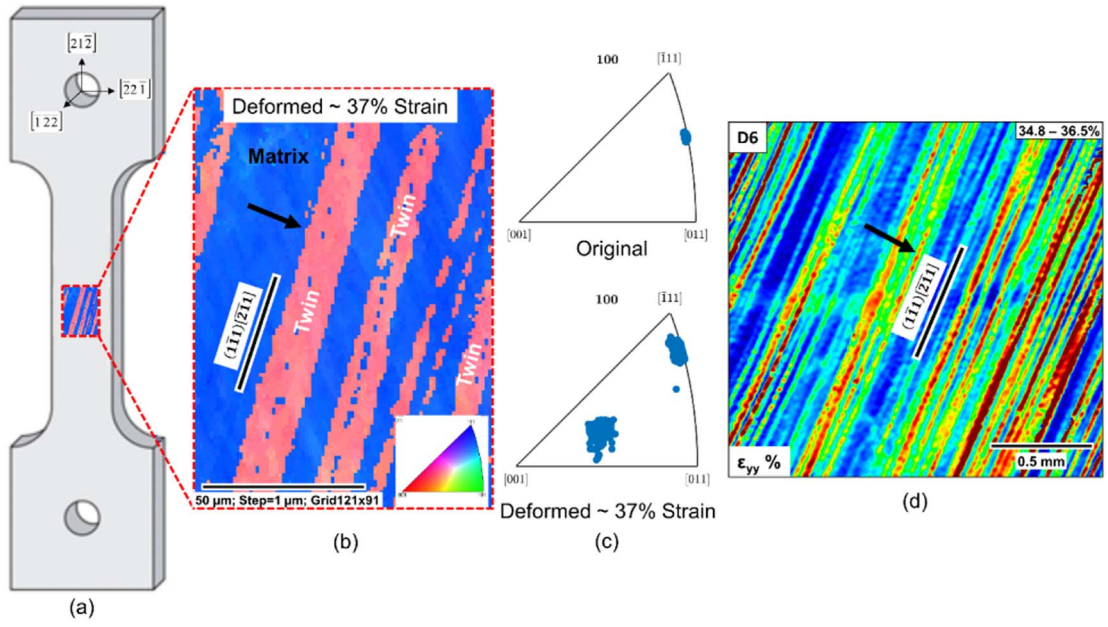

Fig. 10. (a) Schematic of the ⟨122⟩ tension sample presented in Fig. 9. (b) EBSD map taken at the center of the sample. Clear twinning formation is observed with a 60° degree misorientation between the matrix and twin. (c) The corresponding IPFs for the original orientation and the EBSD map shown in (b). DIC contour plot of the ε_{yy} normal strains.

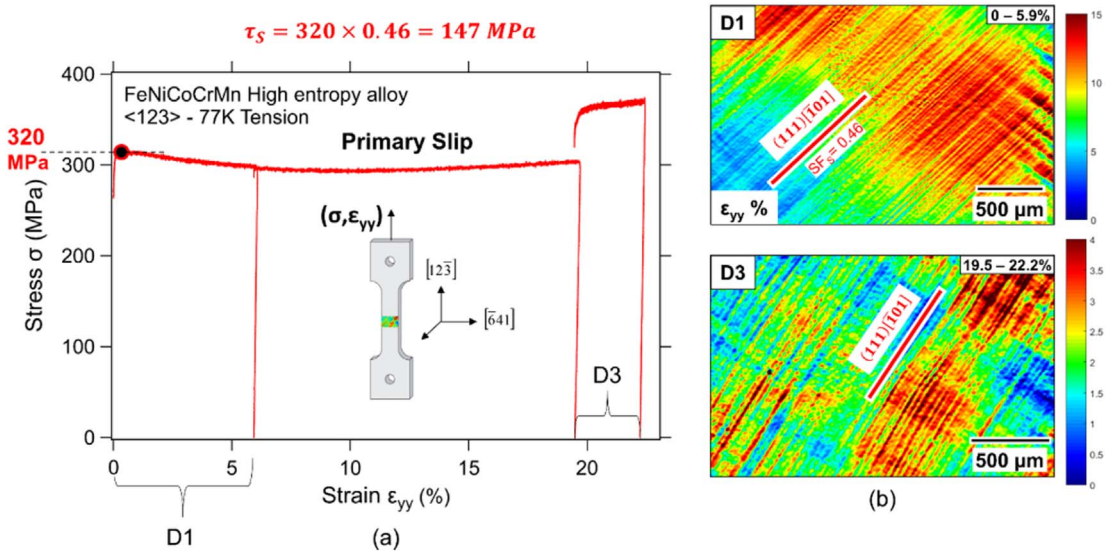

Fig. 11. (a) Incremental stress-strain response for a ⟨123⟩ single crystal loaded at 77 K. (c) Selected contour plots showing the normal strain fields ε_{yy} along the loading for D1 and D3. The localizations and strain bands in D1 were associated slip activity on the (111) slip plane.

Table 4
Schmid factors for ⟨123⟩ single crystal (based on original crystal orientation from EBSD orientation data). The activated slip system for the sample discussed in Fig. 11 is highlighted in the table.

Slip system	Schmid factor - slip	Schmid factor - twin	Twin system
(111)[$\bar{1}$01]	**0.46**	0.48	(111)[$\bar{2}$11]
(111)[1$\bar{1}$0]	0.37	− 0.16	(111)[1$\bar{2}$1]
(111)[0$\bar{1}$1]	0.09	− 0.32	(111)[11$\bar{2}$]
($\bar{1}\bar{1}$1)[0$\bar{1}\bar{1}$]	0.27	− 0.04	($\bar{1}\bar{1}$1)[2$\bar{1}$1]
($\bar{1}\bar{1}$1)[$\bar{1}$0$\bar{1}$]	0.10	0.25	($\bar{1}\bar{1}$1)[$\bar{1}$21]
($\bar{1}\bar{1}$1)[1$\bar{1}$0]	0.17	− 0.21	($\bar{1}\bar{1}$1)[$\bar{1}\bar{1}\bar{2}$]
(1$\bar{1}$1)[0$\bar{1}\bar{1}$]	0.04	− 0.01	(1$\bar{1}$1)[$\bar{2}\bar{1}$1]
(1$\bar{1}$1)[$\bar{1}$01]	0.03	− 0.03	(1$\bar{1}$1)[121]
(1$\bar{1}$1)[$\bar{1}\bar{1}$0]	0.01	0.04	(1$\bar{1}$1)[1$\bar{1}\bar{2}$]
($\bar{1}$11)[$\bar{1}$0$\bar{1}$]	0.33	0.30	($\bar{1}$11)[211]
($\bar{1}$11)[$\bar{1}\bar{1}$0]	0.19	− 0.03	($\bar{1}$11)[$\bar{1}\bar{2}$1]
($\bar{1}$11)[0$\bar{1}$1]	0.14	− 0.27	($\bar{1}$11)[$\bar{1}$1$\bar{2}$]

(compared to clearly exceeding the CRSS as in the ⟨122⟩ sample) which could explain the lack of twinning in this case. The only sample that stood out was the room temperature ⟨111⟩ sample; the sample displayed significant hardening and the resolved stresses are in the range or above the CRSS for the nucleation of twinning as determined at 77 K. The lack of twinning can be attributed, as discussed previously, due to temperature dependence in the CRSS for twinning nucleation. However, this observation can be simply related to the size of deformation twins and the measurement resolution of the techniques adopted in this work. The deformation could have been accommodated by nanotwins as opposed to large scale twining (at the microscale as detected by EBSD or pronounced stress drops in the ⟨122⟩ and ⟨111⟩ 77 K cases in this work). Other researchers have, however, been able to detect densely packed nanotwins using EBSD [2]. In this work, and despite collecting EBSD at multiple magnifications and step sizes down to 0.1 μm, no sign of twinning was observed for the ⟨111⟩ RT sample. Here we also point to some discrepancy in the literature related to the observation of twining above 77 K. In recent TEM analysis on single crystalline ⟨111⟩ FeNiCoCrMn HEA deformed at 298 K, 10–15 nm thick nanotwins were reported [23]. In previous work on polycrystalline FeNiCoCrMn, Otto et al., TEM analysis has shown no signs of twinning for samples deformed at temperatures above 77 K [5]. In summary, with the exception of the RT ⟨111⟩ sample, the results presented in this study seem to support the validity of the Schmid law to predict deformation twinning based on the obtained CRSS for τ_T and Schmid factor for different crystal orientations.

Most of the samples considered in this work displayed different hardening response. The crystal orientation was the dominant factor in introducing the observed differences. For example, the RT ⟨111⟩ sample, experienced significant hardening with stresses increasing from ~170 MPa at yielding to around 720 MPa at ~40% strain ($\frac{d\sigma}{d\varepsilon} \cong 1350\ MPa$). The activation of multiple slip systems was clearly observed in the DIC contour plots shown in Figs. 2 and 3 and was accompanied by localized response and high strain localizations in slip-slip interaction regions as marked in Fig. 3. These interactions and features are known to affect and induce hardening. A similar argument can be made for the ⟨122⟩ sample, but with the localizations and hardening associated with slip-twin interactions ($\frac{d\sigma}{d\varepsilon} \cong 1444\ MPa$). When comparing the previous to the ⟨123⟩ orientation, which was dominated by primary slip with no traces of activation on any other slip plane as shown in the DIC contour plots in Fig. 11, no hardening was observed and the stress decreased with continued loading (*i.e.*, softening). The ⟨149⟩ samples displayed intermediate hardening as compared to the previous two extremes ($\frac{d\sigma}{d\varepsilon} \cong 125{-}250\ MPa$). In each of the two deformation regions observed on the sample's surface (Regions I & II as marked in Fig. 5), the deformation was dominated by single slip. However, significant interaction took place at the interface separating the two regions, which may have induced the observed hardening. The ⟨149⟩ sample deformed at 77 K showed relatively substantial neck formation. The lack of significant hardening (compared to the ⟨111⟩ samples) can explain the tendency for this orientation to form instabilities in the form of necking.

The curved trace features were detected in the ⟨111⟩ sample deformed to very high strains at room temperature. These curvatures, which are marked in the DIC contour plots in Fig. 3 have emerged at strains approaching 35% and were obvious in at least two independent measurements at D11 and D12 in Fig. 3. With the available DIC and EBSD data, a conclusive mechanism leading to these features cannot be determined. However, and based on the shape of these curvatures that seem to connect parallel {111} planes, cross slip would be a candidate. The strong slip interactions on multiple planes can result in the formation of locks, which would consequently necessitate the activation of new slip planes and degradation in the planar slip character that prevails at lower strains. Although TEM was not available in this work, other researchers have shown in room temperature experiments the formation of cell structure at high strains in polycrystalline FeNi-

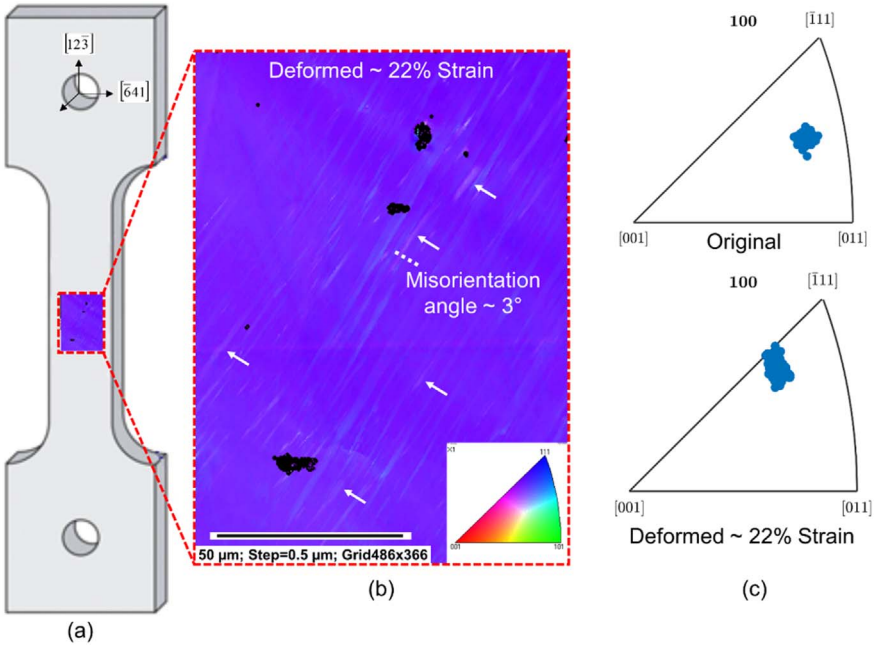

Fig. 12. (a) Schematic of the ⟨123⟩ tension sample presented in Fig. 11. (b) EBSD map taken at the center of the sample. The regions/islands marked with white arrows are related to the surrounding material with a 3° misorientation. (c) The corresponding IPFs for the original orientation and the EBSD map shown in (b).

Table 5
Critical resolved shear stress (CRSS) for slip activation.

Crystal orientation	Deformation temperature	Activated slip Schmid factor	Activation stress (MPa)	CRSS τ_S (MPa)	Average τ_S (MPa)
⟨111⟩	RT	0.31	170	53	$\tau_{S@RT} = 56$
⟨149⟩	RT	0.50	120	60	
⟨149⟩	77 K	0.50	290	145	
⟨122⟩	77 K	0.41	420	172	$\tau_{S@77K} = 155$
⟨123⟩	77 K	0.46	320	147	

CoCrMn HEA (and no twinning) [5]. We also point to a recent work showing a proportional relation between temperature and stacking fault energy for FeNiCoCrMn HEA [24]. An increase in SFE above 77 K can obviously influence the tendency for twining. This aspect requires further investigation and additional TEM analysis focused on the regions displaying the curvatures in the strain bands/traces.

The ⟨149⟩ samples deformed at room temperature and 77 K both displayed the formation of two distinct deformation regions. This orientation had high Schmid factors (~0.5) for two different systems as listed in Table 2. The deformation in each of the regions was dominated by one of the systems only. Based on crystal orientation measurements, EBSD does not point to any orientation difference that would induce such a response (*i.e.*, it is in fact a single crystal and not a bicrystal). The composition analysis through EDX (both maps and line scan) did not point to any heterogeneity in the crystal composition that would explain the formation of two distinct regions that deformed differently. High resolution optical images and SEM images did not pick any special features delineating the interface between the two regions, which only became detectable after deformation. The consistency between the room temperature result (which was repeated twice) and the 77 K, really point to an inherent feature in the crystal (*e.g.*, inclusion, precipitate, or void) potentially inducing the initiation of slip on two different planes in different regions. Additional analysis, potentially using TEM, will be needed to fully understand and explain the formation of an interface separating two region of dissimilar deformation modes. We note, however, that although some sort of crystal defect can induce the formation of what appears to be an interface during deformation, an important outstanding issue remains which is why beyond initiation the deformation was only dominated by primary slip on a single system despite having another slip system with similarly high Schmid factor (which was operative elsewhere in the crystal). The planar slip character and the ability to accommodate large strain on a single system (unimpeded motion of dislocations) combined with lack of significant hardening may have contributed to why each region deformed differently beyond the onset of plasticity. Latent hardening in the form of increased slip resistance for the inactive system in each region can also explain the fact that deformation was dominated by primary slip. This observation motivates further work aimed to quantify how deformation history, and not only orientation, impacts the activation of slip in HEAs.

Table 6
Summary of observed twining and the maximum resolved shear stress RSS for the twin system with the highest Schmid factor. The CRSS for twinning is highlighted in the table.

Crystal orientation	Deformation temp.	Max. twinning Schmid factor	Max. stress during exp. (MPa)	Max. RSS (MPa)	Max. strain during exp. (%)	Twining expected based on Schmid law	Twining observed
⟨111⟩	RT	0.35	720	252	41	Yes	NO
⟨149⟩	RT	0.44	230	101.2	38	NO	NO
⟨111⟩	77 K	0.34	450	**153**	5	Established the CRSS	YES
⟨149⟩	77 K	0.44	340	149	32	NO	NO
⟨122⟩	77 K	0.47	970	455	35	YES	YES
⟨123⟩	77 K	0.48	320	153.6	25	Very close to CRSS	NO

5. Conclusions

The work supports the following conclusions:

1– For FeNiCoCrMn HEA, the CRSS for slip activation has a very strong temperature dependence increasing from ~55 MPa at room temperature to around 150 MPa at 77 K. Such temperature dependence, which is common in BCC alloys, is unusual for FCC alloys. Variation in the CRSS among single crystal orientations was insignificant compared to the difference associated with decreasing the temperature down to 77 K.
2– The activated slip at the onset of plasticity was limited to primary slip on one of the slip systems with high Schmid factors. Primary slip dominated the response for orientations where low hardening was observed. Orientations with relatively higher hardening rates displayed secondary slip as well.
3– Large scale deformation twinning was detected for some of the considered samples at 77 K. For the ⟨111⟩ orientations, the nucleation of twinning was accompanied by a large stress drop with limited prior slip. For the ⟨122⟩ sample, twinning was preceded by considerable slip. Due to low hardening levels, some of the samples deformed at 77 K did not show any signs of twinning. None of the crystals tested at RT displayed detectable twining.
4– Based on the determined CRSS for twin nucleation from the ⟨111⟩ sample and Schmid law, we attributed the lack of twining in some of the samples deformed at 77 K to low stress levels not reaching the experimentally established CRSS for twin nucleation.

Acknowledgements

This research was supported by National Science Foundation grant NSF CMMI-1562288, which is gratefully acknowledged. The corresponding author would like to acknowledge the partial financial support from the American University of Sharjah through the Office of Research and Graduate Studies (FRG16-T-16).

Appendix

The appendix provides the raw EBSD data for the samples studied in this work and how the crystal orientation was determined.

1– Using the Euler angles (φ1, Φ, φ2), the rotation matrix $\boldsymbol{g}$ is determined using the following equation (Bunge definition). This rotation matrix is used to transform between *Sample* and *Crystal* frames (see Fig. 13).

$$\boldsymbol{g} = \begin{bmatrix} \cos\varphi_1\cos\varphi_2 - \sin\varphi_1\sin\varphi_2\cos\Phi & \sin\varphi_1\cos\varphi_2 + \cos\varphi_1\sin\varphi_2\cos\Phi & \sin\varphi_2\sin\Phi \\ -\cos\varphi_1\sin\varphi_2 - \sin\varphi_1\cos\varphi_2\cos\Phi & -\sin\varphi_1\sin\varphi_2 + \cos\varphi_1\cos\varphi_2\cos\Phi & \cos\varphi_2\sin\Phi \\ \sin\varphi_1\sin\Phi & -\cos\varphi_2\sin\Phi & \cos\Phi \end{bmatrix} \tag{A1}$$

2– To transform from sample frame to crystal frame, the following equation are used

$$\boldsymbol{LD_{crystal} = g\, LD_{sample}} \text{ where } \boldsymbol{LD_{crystal}} \text{ and } \boldsymbol{LD_{sample}} \text{ are vectors} \tag{A2}$$

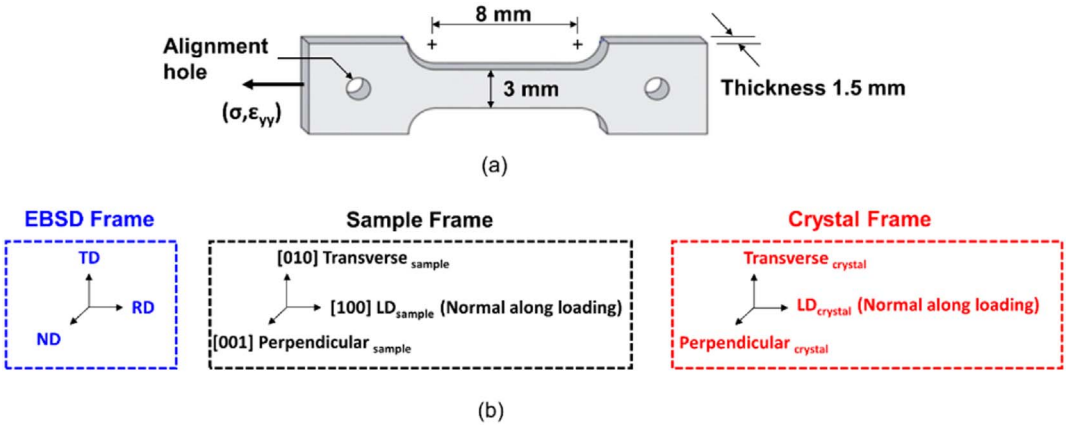

Fig. 13. (a) Schematic of the dogbone tensile sample. (b) EBSD, Sample, and Crystal frames relative to the loading direction.

Table 7
Original crystal orientation from EBSD and the corresponding loading direction in crystal frame.

Sample	Figure	Euler angles			LD_{sample}	$LD_{crystal} = g\, LD_{sample}$	~Corresponding crystal direction
		φ_1	Φ	φ_2			
⟨111⟩	Figs. 1–3	106	138	247	[100]	[−0.55 −0.53 0.64]	$[\bar{1}\,\bar{1}\,1]$
⟨111⟩	Fig. 4	103	145	240	[100]	[−0.58 −0.59 0.56]	$[\bar{1}\,\bar{1}\,1]$
⟨149⟩	Figs. 5–6	323	132	238	[100]	[−0.08 0.89 −0.45]	$[\bar{1}\,9\,\bar{4}]$
⟨122⟩	Figs. 9–10	244	132	207	[100]	[0.66 0.34 −0.67]	$[21\bar{2}]$
⟨123⟩	Figs. 11–12	280	128	222	[100]	[0.28 0.57 −0.78]	$[12\bar{3}]$

3– The sample loading direction was the [100] for all cases. Using the EBSD data, the corresponding direction in crystal frame was calculated using Eqs. (A1) and (A2). The approximate crystal orientations (as used throughout the text) are shown in the last column of Table 7.

References

[1] J.W. Yeh, Recent progress in high-entropy alloys, Ann. Chim. Sci. Mater. (Paris) 31 (2006) 633–648.
[2] B. Gludovatz, A. Hohenwarter, D. Catoor, E.H. Chang, E.P. George, R.O. Ritchie, A fracture-resistant high-entropy alloy for cryogenic applications, Science 345 (2014) 1153–1158.
[3] D.B. Miracle, O.N. Senkov, A critical review of high entropy alloys and related concepts, Acta Mater 122 (2017) 448–511.
[4] Z.P. Lu, H. Wang, M.W. Chen, I. Baker, J.W. Yeh, C.T. Liu, T.G. Nieh, An assessment on the future development of high-entropy alloys: summary from a recent workshop, Intermetallics 66 (2015) 67–76.
[5] F. Otto, A. Dlouhý, C. Somsen, H. Bei, G. Eggeler, E.P. George, The influences of temperature and microstructure on the tensile properties of a CoCrFeMnNi high-entropy alloy, Acta Mater 61 (2013) 5743–5755.
[6] B. Gludovatz, E.P. George, R.O. Ritchie, Processing, microstructure and mechanical properties of the CrMnFeCoNi high-entropy alloy, JOM 67 (2015) 2262–2270.
[7] Z. Zhang, M.M. Mao, J. Wang, B. Gludovatz, Z. Zhang, S.X. Mao, E.P. George, Q. Yu, R.O. Ritchie, Nanoscale origins of the damage tolerance of the high-entropy alloy CrMnFeCoNi, Nat Commun 6 (2015) 10143.
[8] G. Laplanche, A. Kostka, O.M. Horst, G. Eggeler, E.P. George, Microstructure evolution and critical stress for twinning in the CrMnFeCoNi high-entropy alloy, Acta Mater 118 (2016) 152–163.
[9] R. Raghavan, C. Kirchlechner, B.N. Jaya, M. Feuerbacher, G. Dehm, Mechanical size effects in a single crystalline equiatomic FeCrCoMnNi high entropy alloy, Scr Mater 129 (2017) 52–55.
[10] C. Zhu, Z.P. Lu, T.G. Nieh, Incipient plasticity and dislocation nucleation of FeCoCrNiMn high-entropy alloy, Acta Mater 61 (2013) 2993–3001.
[11] F. Otto, N.L. Hanold, E.P. George, Microstructural evolution after thermomechanical processing in an equiatomic, single-phase CoCrFeMnNi high-entropy alloy with special focus on twin boundaries, Intermetallics 54 (2014) 39–48.
[12] W. Woo, E.W. Huang, J.-W. Yeh, H. Choo, C. Lee, S.-Y. Tu, In-situ neutron diffraction studies on high-temperature deformation behavior in a CoCrFeMnNi high entropy alloy, Intermetallics 62 (2015) 1–6.
[13] D. Barbier, N. Gey, S. Allain, N. Bozzolo, M. Humbert, Analysis of the tensile behavior of a TWIP steel based on the texture and microstructure evolutions, Mater Sci Eng A 500 (2009) 196–206.
[14] O. Bouaziz, S. Allain, C.P. Scott, P. Cugy, D. Barbier, High manganese austenitic twinning induced plasticity steels: a review of the microstructure properties relationships, Curr. Opinion Solid State Mater. Sci. 15 (2011) 141–168.
[15] D.R. Steinmetz, T. Jäpel, B. Wietbrock, P. Eisenlohr, I. Gutierrez-Urrutia, A. Saeed–Akbari, T. Hickel, F. Roters, D. Raabe, Revealing the strain-hardening behavior of twinning-induced plasticity steels: Theory, simulations, experiments, Acta Mater. 61 (2013) 494–510.
[16] I. Karaman, H. Sehitoglu, K. Gall, Y.I. Chumlyakov, H.J. Maier, Deformation of single crystal Hadfield steel by twinning and slip, Acta Mater 48 (2000) 1345–1359.
[17] L. Patriarca, A. Ojha, H. Sehitoglu, Y.I. Chumlyakov, Slip nucleation in single crystal FeNiCoCrMn high entropy alloy, Scr Mater 112 (2016) 54–57.
[18] L. Patriarca, W. Abuzaid, H. Sehitoglu, H.J. Maier, Y. Chumlyakov, Twin nucleation and migration in FeCr single crystals, Mater Charact 75 (2013) 165–175.
[19] W. Abuzaid, H. Sehitoglu, J. Lambros, Plastic strain localization and fatigue microcrack formation in Hastelloy X, Mater Sci Eng A 561 (2013) 507–519.
[20] J. Carroll, W. Abuzaid, J. Lambros, H. Sehitoglu, An experimental methodology to relate local strain to microstructural texture, Rev. Sci. Instrum. 81 (2010) 083703.
[21] Z. Wu, H. Bei, G.M. Pharr, E.P. George, Temperature dependence of the mechanical properties of equiatomic solid solution alloys with face-centered cubic crystal structures, Acta Mater 81 (2014) 428–441.
[22] M.A. Meyers, O. Vöhringer, V.A. Lubarda, The onset of twinning in metals: a constitutive description, Acta Mater 49 (2001) 4025–4039.
[23] I. Kireeva, Y. Chumlyakov, Z. Pobedennaya, D. Kuksgauzen, I. Karaman, H. Sehitoglu, Mechanisms of plastic deformation in [1¯11]-oriented single crystals of FeNiMnCrCo high entropy alloy, AIP Conf. Proc. 1783 (2016) 020090.
[24] S. Huang, W. Li, S. Lu, F. Tian, J. Shen, E. Holmström, L. Vitos, Temperature dependent stacking fault energy of FeCrCoNiMn high entropy alloy, Scr Mater 108 (2015) 44–47.